Materials Horizons

ROYAL SOCIETY OF CHEMISTRY

COMMUNICATION

View Article Online
View Journal | View Issue

Cite this: *Mater. Horiz.*, 2025, **12**, 9211

Received 11th April 2025,
Accepted 22nd July 2025

DOI: 10.1039/d5mh00679a

rsc.li/materials-horizons

Environmentally responsive semi-interpenetrating network microcapsules with enhanced stability for corrosion protection†

Hongda Zhou, ‡*[abe] Zexi Shao,‡[ab] Danila V. Ermolin, [c] Alexander S. Novikov,[c] Ekaterina V. Skorb, [c] Rui Cheng,[d] Dmitry G. Shchukin *[e] and Huaiyuan Wang *[ab]

Dynamic, responsive microcapsules present innovative solutions for mitigating corrosion and environmental challenges associated with CO_2 capture, utilization, and storage. For their prospective integration into practical applications, these microcapsules must possess structures that optimally balance responsiveness and structural integrity under harsh acidic environments. Here, we report robust pH-responsive microcapsules (RRMCs) that are synthesized using a dynamic complexation–diffusion assembly approach, incorporating polyelectrolytes of varying molecular weights. The RRMCs feature high encapsulation efficiency (~86%), enhanced stability and sustained controlled release capabilities (up to 14 days). The use of the RRMCs for the controlled release of small molecules, such as benzotriazole (BTA, a widely employed corrosion inhibitor), is demonstrated. The programmed and controlled pH-dependent release behaviour of BTA provides effective protection of metal substrates in an acidic environment. Furthermore, theoretical calculations elucidate the relationship between controlled release and the adsorption mechanism. This strategy offers substantial advancements in the development of responsive microcapsule systems for applications in CO_2-related corrosion control and material durability in harsh environments.

New concepts

Corrosion is a critical challenge in CO_2 capture, utilization, and storage (CCUS) applications, where acidic and supercritical CO_2 environments accelerate material degradation, compromising infrastructure integrity and increasing operational costs. As industries transition to sustainable energy solutions, mitigating corrosion is essential for ensuring long-term reliability. However, conventional corrosion inhibitors suffer from issues such as substantial quantity, low efficiency, and environmental toxicity. Our research reveals robust pH-responsive microcapsules (RRMCs) as a novel solution for corrosion protection in harsh environments. These microcapsules enable precise, stimuli-responsive release of protective agents, enhancing material durability while minimizing chemical waste and environmental impact. By integrating polyelectrolytes of varying molecular weights through a complexation–diffusion assembly strategy, these microcapsules achieve both structural stability and responsive adaptability. This innovation not only advances corrosion control in sustainable energy applications, but also paves the way for broader applications in material durability and environmental protection. By reducing the environmental footprint of corrosion inhibitors and improving energy infrastructure longevity, our approach supports global energy sustainability initiatives. The findings of this study contribute to the broader goal of developing adaptive materials that align with global sustainability efforts in energy science and technology.

Introduction

Corrosion poses a significant challenge in CO_2 capture, utilization, and storage (CCUS) systems, as acidic and supercritical CO_2 environments accelerate material degradation, threatening infrastructure integrity and increasing operational risks.[1,2] The conventional corrosion control methods, such as corrosion inhibitors, are effective but suffer from environmental concerns such as toxicity, bioaccumulation, and uncontrolled release, resulting in inefficiencies and ecological risks.[3,4] To address these limitations, responsive microcapsules have emerged as a promising solution, enabling the controlled and stimuli-responsive release of inhibitors, thereby enhancing protection while reducing chemical consumption and environmental impacts.[5–8] These smart microcapsules adapt to environmental stimuli (*e.g.*, light, temperature, pH, ion strengths), dynamically

[a] *School of Chemical Engineering and Technology and State Key Laboratory of Chemical Engineering and Low-Carbon Technology, Tianjin University, Tianjin 300350, P. R. China. E-mail: hongdazhou_94@tju.edu.cn, huaiyuanwang@tju.edu.cn*
[b] *Tianjin Key Laboratory of Chemical Process Safety and Equipment Technology, Tianjin University, Tianjin 300072, P. R. China*
[c] *ITMO University, 9, Lomonosov Street, Saint Petersburg 191002, Russia*
[d] *Gulliver CNRS UMR 7083, PSL Research University, ESPCI Paris, 10 Rue Vauquelin, Paris 75005, France*
[e] *Stephenson Institute for Renewable Energy, University of Liverpool, Liverpool L69 7ZF, UK. E-mail: shchukin@liverpool.ac.uk*

† Electronic supplementary information (ESI) available. See DOI: https://doi.org/10.1039/d5mh00679a

‡ H. Z. and Z. S. contributed equally to this work.

adjusting their physical properties in an adaptive manner for improved performance.[9,10] However, existing capsule technologies face challenges related to stability, durability, and precise release regulation under extreme CCUS conditions, all of which hinder their scalability and efficiency in practical applications.[11,12] Hence, advancing microcapsule design to achieve both high sensitivity and structural robustness is crucial for developing sustainable corrosion mitigation strategies that ensure long-term infrastructure reliability while minimizing environmental impact.

Interfacial complexation techniques, such as layer-by-layer (LBL) assembly, have emerged as flexible methods for creating coatings on various substrates, involving charged components like polyelectrolytes, colloidal particles, and surfactants.[13–15] Multi-layered polyelectrolyte networks, driven by electrostatic, covalent, or supramolecular interactions, have proven effective for coating diverse surfaces.[16–18] These LBL layers offer a range of functionalities, including responsive behaviours and gas absorption, owing to the variety of polyelectrolytes and nanostructured architectures involved. By exploiting the interfacial assembly of complementary polyelectrolytes on spherical surfaces, responsive microcapsules can be engineered for diverse applications, including drug delivery,[19] self-healing materials,[20] and biosensors.[21] While the rapid electrostatic complexation facilitates the simple and cost-effective deposition of coatings, this swift formation presents challenges in controlling structural parameters such as shell thickness, permeability, and stability, which may limit the efficacy of controlled release systems.

The introduction of interpenetrating structures in the assembly process may provide a promising approach to enhance the structural stability and functionality of polyelectrolyte-based microcapsules.[22,23] By interpenetrating two or more polymer networks, these systems offer improved mechanical strength and structural integrity, which are critical for applications requiring long-term performance in complex environments. Polyelectrolytes, with their diverse functional groups, provide abundant sites for interaction, enabling the formation of interpenetrating bonds through electrostatic, hydrogen bonding, or covalent crosslinking.[24,25] While increased crosslinking or network entanglement improves the mechanical stability of microcapsules, it concurrently diminishes their responsiveness to external stimuli.[26–28] Balancing stability and responsiveness remain a major challenge, especially in controlled-release applications where microcapsules need to preserve their structure while enabling reliable release.

Herein, we demonstrate the fabrication of RRMCs to achieve high stability and sustainable controlled release capabilities (Fig. 1). A strategy combining interfacial complexation and diffusion crosslinking is employed to deposit responsive interpenetrating polyelectrolyte networks on hollow mesoporous silica (HMS) skeletons. The polyelectrolyte shells consist of low-molecular-weight polycations, branched poly(ethylenimine) (bPEI), and high-molecular-weight polyanions, poly(acrylic acid) (PAA). The microcapsules exhibit reversible pH responsiveness owing to the dynamic protonation, allowing the shell to swell in acidic pH (≤ 4)

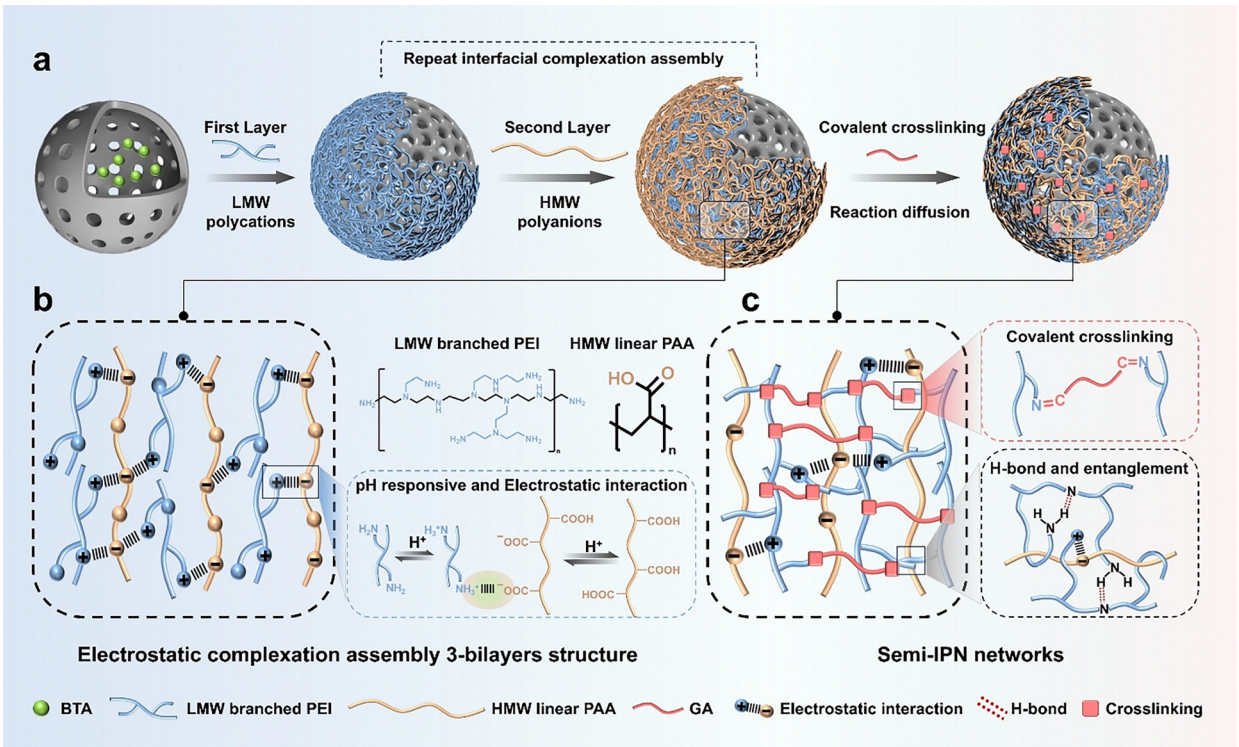

Fig. 1 Assembly of polyelectrolyte semi-interpenetrating microcapsules. (a) Schematic illustration of the synthesis of RRMCs *via* interfacial electrostatic complexation assembly and crosslinking. (b) Schematic depiction of electrostatic complexation between low-molecular-weight bPEI and high-molecular-weight PAA. (c) The formation of interpenetrating networks initiated from reaction diffusion and covalent crosslinking process.

and contract at higher pH levels (Fig. 1b). Further reaction–diffusion processes and crosslinking with glutaraldehyde induce the formation of interpenetrating networks that enhance both stability and mechanical strength. Compared to previous studies employing conventional polyelectrolyte pairs such as PAH, PAA, and PSS, our approach introduces a new assembly strategy based on polyelectrolytes with different molecular weights.[29,30] The integrated interfacial complexation and diffusion crosslinking methods enable improved control over capsule architecture and performance. The controlled release behaviours were monitored and analysed by using BTA as a model small molecule. The controlled release and adsorption mechanisms were explored through density functional theory (DFT) calculations. This study provides a new framework for designing robust, responsive microcapsules for controlled release applications, such as corrosion inhibition. The proposed microcapsules hold considerable potential for enhancing the efficiency and sustainability of corrosion inhibitors in large-scale carbon utilization and storage, contributing to improved environmental practices.

Results and discussion

Fabrication and structure of RRMCs

The robust responsive microcapsules were constructed using an interfacial complexation strategy applied to HMS skeletons. HMSs were prepared *via* a sol–gel/emulsion synthesis route, employing TEOS as the silica source to simultaneously generate the internal cavity and provide mechanical integrity to the shell structure.[31] The HMSs exhibit a uniform spherical morphology with well-defined hollow cavities (Fig. 2a). Nitrogen adsorption–desorption analysis reveals a typical type IV isotherm with a hysteresis loop, indicating the BET surface area of approximately 840 $m^2\ g^{-1}$, the pore size of 3.91 nm, and the shell thickness of around 44 nm (Fig. 2a and d). These results confirm the mesoporous structure of the HMSs, which provide ample internal space for encapsulation and channels for the release of small molecules. Upon loading with BTA, oppositely charged polyelectrolytes were sequentially deposited on the HMSs through an interfacial complexation and reaction–diffusion strategy,[32] resulting in the formation of robust responsive

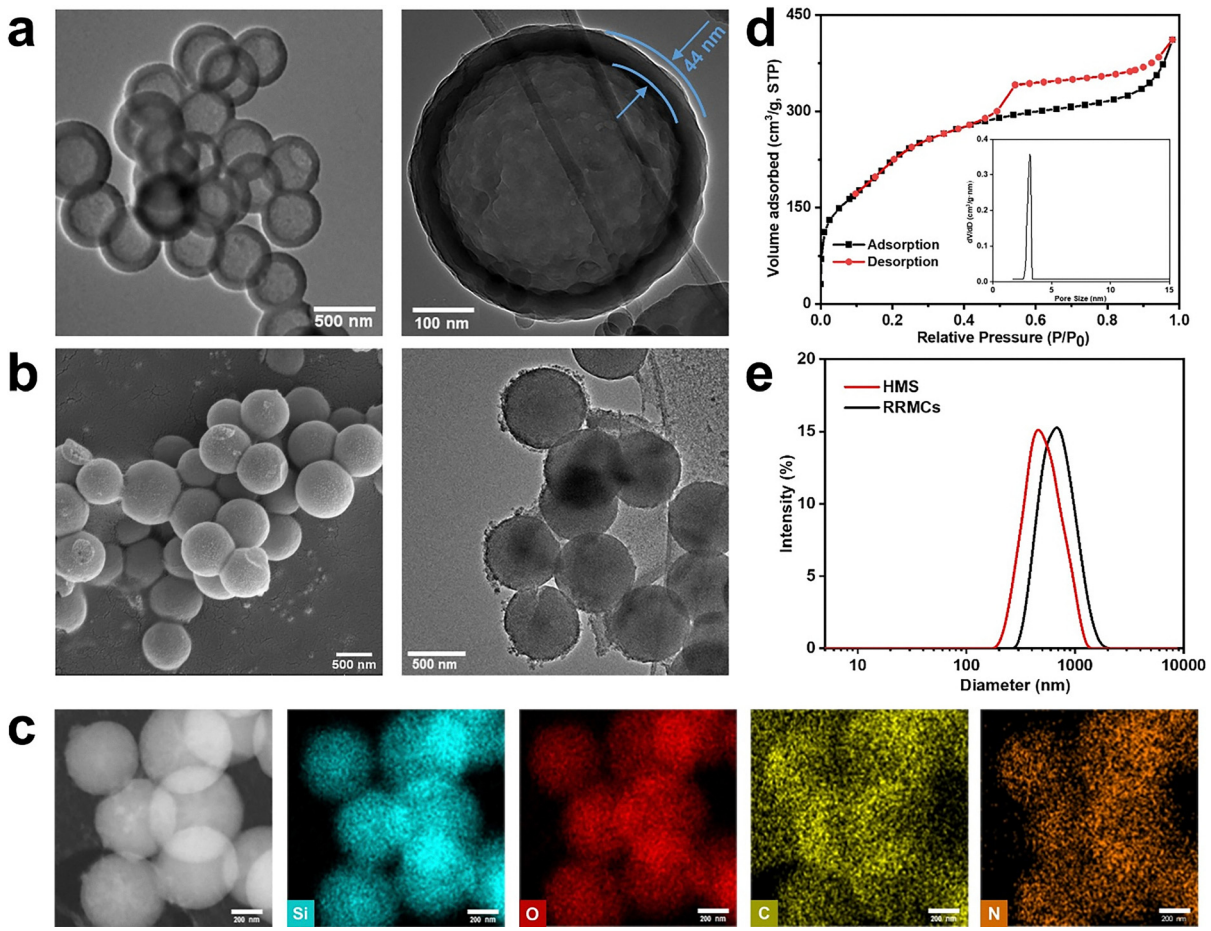

Fig. 2 Fabrication and morphology characterization of RRMCs. (a) TEM images of the HMS with diameters of about 459 nm. (b) SEM and TEM images of the RRMCs with diameters of about 728 nm. (c) STEM image of the RRMCs and the corresponding element distribution mapping. (d) N_2 adsorption–desorption isotherms and the corresponding pore size distribution plots of HMS. (e) Hydrodynamic diameter distribution of HMS and RRMCs.

microcapsules. The multi-layered polyelectrolyte coatings were achieved by alternately depositing bPEI and PAA. When bPEI comes into contact with PAA, a layered complex forms immediately, driven by strong electrostatic interactions.[33] The bPEI molecules then diffuse across the layered complex, with the branched NH_3^+ groups entangling with the long PAA chains, thereby creating interpenetrating networks and increasing the coating thickness (Fig. 1c). Zeta potential measurements show that the HMSs exhibit stable negative values, ranging from −40 to −50 mV across the entire pH range, while the zeta potentials of bPEI and PAA range from +58 to +10 mV and −20 to −40 mV, respectively, within a pH range of 4 to 10 (Fig. S1, ESI†). The desired number of layers in the responsive microcapsules was controlled by adjusting the pH of the deposition solutions. The variation in zeta potential of the polyelectrolytes as a function of the number of layers confirms the successful formation of multilayer polyelectrolyte coatings. Upon reaching the desired number of layers, bPEI continues to diffuse across the assembled layers, interacting with PAA and contributing to the development of increasingly entangled networks. These networks are subsequently crosslinked with glutaraldehyde, resulting in the formation of interpenetrating polyelectrolyte networks with significantly enhanced stability. Thermogravimetric analysis of the RRMCs indicates that a temperature of at least 200 °C is required to induce a substantial mass loss (Fig. S2, ESI†). The RRMCs display a smooth, uniform spherical morphology with an average diameter of approximately 728 nm (Fig. 2b and e). Energy-dispersive X-ray elemental mapping reveals a homogeneous distribution of carbon (C), nitrogen (N), oxygen (O), and silicon (Si) throughout the microcapsules, confirming the integrated structure of the RRMCs (Fig. 2c). These results demonstrate the successful fabrication of microcapsules with well-defined structural characteristics, making them potential candidates for controlled release applications.

Stability and responsiveness of RRMCs

The pH-responsive behaviour of the RRMCs arises from the dynamic protonation of functional groups within the interpenetrating polyelectrolyte coatings, enabling reversible swelling and contraction of the polymer networks.[34] The typical FTIR spectrum of the RRMCs reveals key chemical features (Fig. 3a). A broad absorption peak between 3360 and 3500 cm^{-1} corresponds to the stretching vibrations of hydroxyl (–OH) and secondary amine (N–H) groups. The absorption band at 1655, attributed to the C=N bond vibration, signifies the formation of covalent bonds *via* the Schiff base reaction between glutaraldehyde (GA) and bPEI (Fig. S3, ESI†). Additional peaks at 1560 and 1403 cm^{-1} correspond to the stretching vibrations of C–N

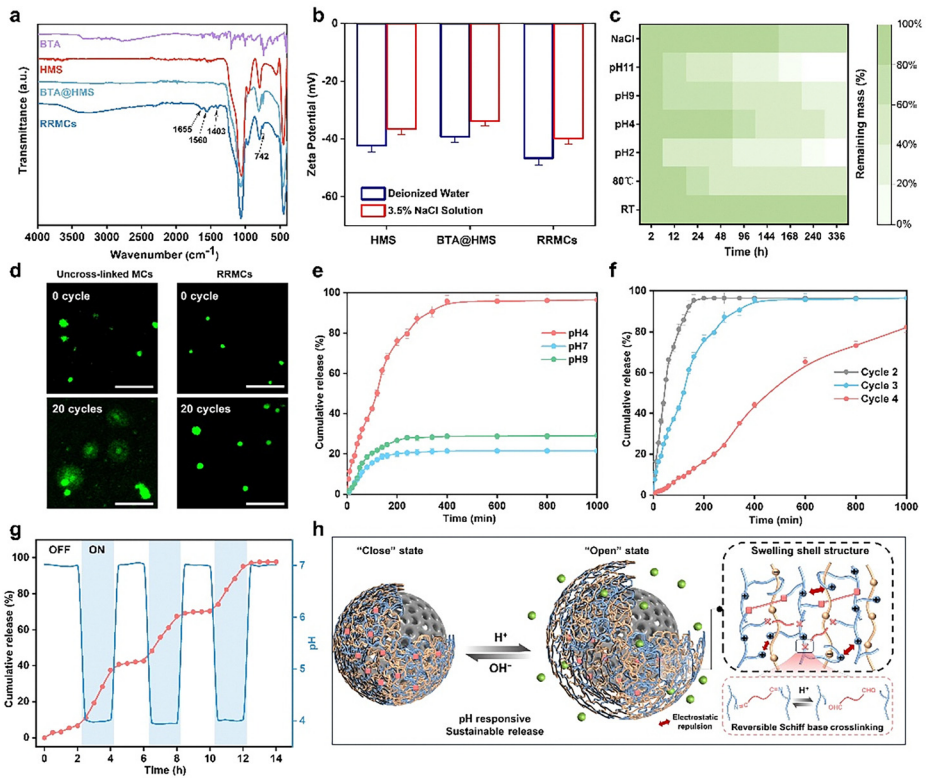

Fig. 3 Stability and responsiveness of RRMCs. (a) FT-IR spectra. (b) Zeta potential variety of different samples in DI water and NaCl solutions. (c) Heat maps showing the mass changes of 3-bilayer polyelectrolyte coatings after incubation in different media over 14 days. (d) CLSM images of uncross-linked MCs and RRMCs after 20 pH responsive swelling–deswelling cycles. (e) Cumulative release of BTA from RRMCs at different pH values at room temperature. (f) Cumulative release of BTA from RRMCs prepared using different deposition cycles (one deposition cycle consists of two assembly steps, forming a bilayer bPEI/PAA). (g) The release profile of BTA from RRMCs under periodic pH changes. (h) Schematic depiction of the pH responsive release behaviour and reversible structure change of polyelectrolyte networks.

groups and carboxyl (–COOH) groups, respectively. These spectral features reveal the successful deposition and covalent crosslinking of the polyelectrolyte networks. The encapsulation and loading efficiencies of BTA within the microcapsules are provided in Fig. S4 (ESI†). The loading efficiency increases with the BTA-to-HMS weight ratio, although the encapsulation efficiency decreases at the highest weight ratio (5 : 5). For consistency in subsequent experiments, a BTA-to-HMS weight ratio of 4 : 5 was selected.

The zeta potential of the RRMCs remains relatively stable at approximately −40 mV in both deionized water and NaCl solutions (Fig. 3b). The stability of the polyelectrolyte networks was evaluated by tracking mass changes in various environments, including deionized water (at room temperature and 80 °C), solutions of varying pH, and 3.5 wt% NaCl (Fig. 3c). The polyelectrolyte networks exhibit high stability during the first two hours in all solutions, indicating the enhanced robustness of the interpenetrating structures. Notably, the networks retain over 75% stability in highly acidic (pH 2) and basic (pH 11) conditions for up to 12 hours, whereas uncrosslinked polyelectrolyte coatings dissolve within one hour. The presence of NaCl increases ionic strength, facilitating the rapid diffusion and reaction of both intrinsic and extrinsic bonds, thereby further enhancing the entanglement strength and stability of the polyelectrolyte networks.[35] The reversible cycling stability of the RRMCs was visualized by monitoring morphological changes using CLSM (Fig. 3d). Following 20 cycles of pH-induced swelling and shrinking, microcapsules without crosslinked polyelectrolyte layers begin to break apart, and the released polymers form large aggregates. In contrast, RRMCs remain intact, highlighting the stabilizing effect of their crosslinked and entangled polymer networks (Fig. 3h). The force–deformation (F–δ) curve of the RRMCs indicates mechanical reinforcement of the hybrid shells, with a calculated reduced modulus of 1345 MPa (Fig. S5, ESI†).

Responsive microcapsules have recently been explored for controlled release applications.[36,37] Here, the controlled release of BTA from RRMCs was investigated. UV-vis absorption spectra of BTA at varying pH values were analysed, and calibration curves were established to quantify released BTA concentrations (Fig. S5, ESI†). The release profile exhibits clear pH-responsive behaviour, with up to 98.93% of BTA released in an acidic environment (pH 4, Fig. 3e and Fig. S7, ESI†). This behaviour is driven by the pH-dependent permeability of the polyelectrolyte shells. At pH 4, the carboxyl group of PAA is largely protonated with less charge. The structures undergo a swelling transition with higher permeability due to the electrostatic repulsion upon protonation of the highly charged amine groups from bPEI.[38–40] Electrostatic repulsion between protonated amine groups of bPEI further loosens the network, facilitating the release of encapsulated small molecules (Fig. 3h). The release behaviour of RRMCs can be modulated by varying the number of polyelectrolyte layers through different deposition cycles (one deposition cycle consisting of two assembly steps, forming a bilayer of bPEI/PAA), which alters their permeability. RRMCs with four deposition cycles exhibit more sustained release profiles compared to those with two cycles (Fig. 3f). Increasing cycles lead to an increase in the thickness of polyelectrolyte networks, resulting in a denser interpenetrating structure and reduced permeability. The CLSM images and fluorescence intensity profiles show that more deposition cycles lead to larger microcapsules with higher fluorescence intensity (Fig. S10, ESI†). The number of polyelectrolyte layers also affects the storage stability of the RRMCs (Fig. S11, ESI†). Furthermore, the sustainable release of BTA can be tuned by exploiting the pH responsiveness of the polyelectrolyte networks (Fig. 3g). The controlled switching between "open" and "closed" states is driven by reversible structural changes in the network, enabling sustainable controlled release applications.

The RRMCs demonstrate promising material sustainability due to their robust, reversible structural integrity and tunable performance. The crosslinked and entangled polyelectrolyte networks maintain morphological and mechanical stability over repeated pH-triggered cycles, reducing degradation and material loss. Additionally, the ability to modulate permeability and release profiles through controlled layer deposition enhances functional longevity. These features, combined with their reversible responsiveness and sustained release capabilities, support the development of durable, reusable systems for long-term controlled release applications, aligning well with principles of sustainable material design.

Application of RRMCs for controlled-release corrosion inhibition

Stimuli-responsive microcapsules with self-regulated release behaviours have found applications in various chemical engineering applications.[41–43] For instance, acidic corrosion is a common issue during CO_2 capture, transportation, and utilization.[44–46] Here, we explore the promising corrosion inhibition of RRMCs for carbon steel, serving as an example of responsive microcapsule applications. To evaluate the enhanced controlled release capabilities of RRMCs, electrochemical testing was performed under simulated pH conditions. Open-circuit potential (OCP) measurements were conducted in three different electrolytes (with and without RRMCs) in pH 4, 7, and 9 NaCl solutions, with OCP values shifting towards the anode potentials (Fig. S12, ESI†). In the presence of RRMCs, the variation in anode potential was more pronounced at higher pH values (0.2 V *vs.* SHE at pH 9) compared to the blank solution. Over time, the OCP values were stabilized after 1800s of immersion, indicating the formation of a corrosion barrier (*i.e.*, organic or passive film), which reduces the active surface area available for electrochemical reactions.[47,48] In the Nyquist plots for pH 4-RRMC samples, the semicircle radius initially decreases and subsequently increases, indicating a controlled release of BTA under acidic conditions (Fig. 4a). Notably, the radius for pH 7-RRMC samples increases with time, while for pH 9-RRMCs, it initially increases and then decreases (Fig. 4b and c). This behaviour is attributed to the accumulation of corrosion products and the passive behaviour on the substrate under alkaline conditions. The carbon steel samples were exposed to simulated industrial conditions with and without RRMCs in a 3.5 wt% NaCl solution for 20 days to assess the smart release and long-term protective capabilities (Fig. 4d). The enlarged SEM images clearly depict the swollen microcapsules and their extensive coverage on the metal surface, alongside a notable reduction

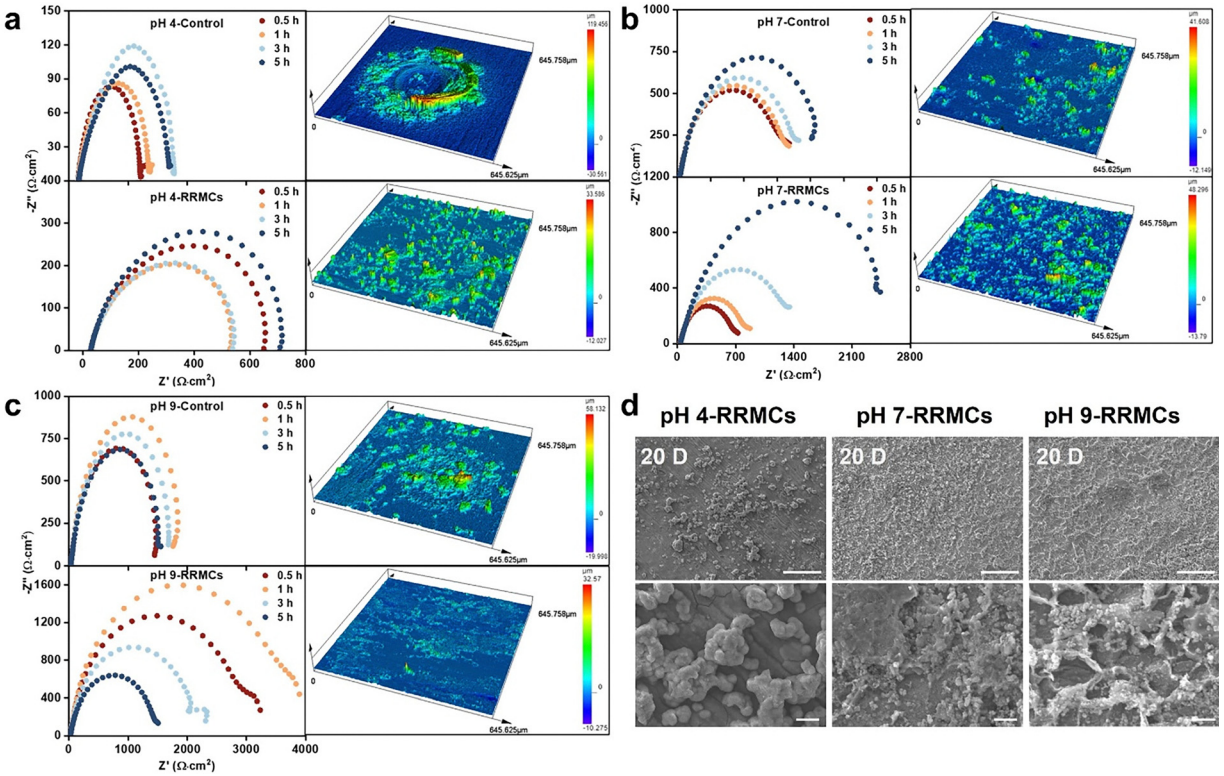

Fig. 4 Application of RRMCs for controlled-release corrosion inhibition. Nyquist plots and correspond optic images of carbon steel in the absence and presence of RRMCs: (a) pH 4, (b) pH 7, (c) pH 9, (d) SEM images after immersion for 20 days in the presence of RRMCs (upper), the enlarge images (lower), scale bar 50 μm (upper), lower 5 μm (lower).

in corrosion products under acidic conditions. Optical images clearly show higher number of pits and corrosion products on the carbon steel surface of control samples in the blank solution. In contrast, the samples in the presence of RRMCs exhibit a more homogeneous surface with significantly reduced corrosion (yellow stains in optical images, Fig. S13, ESI†), indicating that RRMCs provide long-term protection by forming a stable corrosion barrier under extreme industrial conditions. To investigate the anodic and cathodic corrosion kinetics, Tafel testing was conducted (Fig. S14, ESI†). In the presence of RRMCs in pH 4 electrolyte, cathodic current densities were lower compared to the blank solution (Table S1, ESI†). SEM images after Tafel testing visually confirm the corrosion inhibition effect (Fig. S15, ESI†). These results suggest that RRMCs function as anodic inhibitors in the anode regions,[49] and their incorporation into more aggressive industrial environments may alter corrosion kinetics, thereby enhancing resistance to localized corrosion.

Comprehensive electrochemical impedance spectroscopy (EIS) analysis was conducted to further confirm the smart controlled-release and robust corrosion inhibition properties. The EIS data for pH-control and pH-RRMC samples (Fig. 4) show that the arc radius of capacitive reactance for the RRMC group increases from 0.5 h to 5 h, indicating gradual formation of a protective film on the carbon steel surface. Additionally, the phase angle shifts toward higher frequencies, with the peak of the phase angle increasing and then decreasing (Fig. S16, ESI†), further demonstrating that RRMCs reduce the corrosion rate of carbon steel. The electron transfer resistance (R_{ct}), obtained by fitting the EIS data to an equivalent circuit (Fig. S17, ESI†), shows that variations in R_{ct} with immersion time reflect the smart controlled-release process under more aggressive industrial conditions (Table S2, ESI†). To further investigate the relationship between the inhibition mechanism and corrosion behaviour of RRMCs, EDS and XPS were used to analyse the surface chemistry of the protective film on the carbon steel surface. EDS results reveal the presence of Si and O elements on the pH 4-RRMCs-treated surface, suggesting that released BTA interacts with Fe or its oxide to form a protective film (Fig. S18, ESI†). Although no N element was detected by EDS, XPS analysis identified N on the carbon steel surface, particularly in flat regions (Fig. S19, ESI†). This indicates that BTA interacts with Fe through its N atom, forming a thin protective film at the flat regions and engaging with Fe(II), Fe(III) or other metal impurities to form a monolayer or sub-monolayer.[50] The absence of such peaks on other specimens provides strong evidence that RRMCs effectively reduce the Fe corrosion rate through their pH-controlled release capacity. Together, these results confirm that RRMCs can form a protective barrier even under acidic environmental conditions.

Molecular release and absorption modeling

The theoretical simulations were employed to investigate the continuous interconnected process of BTA release from RRMCs and its adsorption onto the Fe surface. To elucidate the molecular release mechanism, we utilized a simplified model

in which PAA and bPEI were represented as three-chain polymeric fragments. The association Gibbs free energies of these model systems with BTA were then calculated (see Supplementary Methods in the ESI† for details). Since association of Gibbs free energies of PAA and bPEI with BTA can be strongly influenced by conformational preferences, we performed a preliminary conformational search and considered not only the most energetically favourable conformer but also higher-energy conformers in our calculations.[51] This conformational search was carried out for both the model polymers (PAA, bPEI) and their supramolecular complexes with BTA. For Gibbs free energy calculations, we employed the r2SCAN-3c composite method, which was previously demonstrated to be reliable for supramolecular systems.[52] To further validate our results, we performed additional DFT computations using the range-separated hybrid functional wB97X-D3BJ in combination with the ma-def2-TZVP basis sets, ensuring accurate treatment of dispersion interactions.[53,54] The resulting association Gibbs free energies of PAA and bPEI with BTA (ΔG_{assoc}) calculated using both methods are shown in Fig. 5a. The association Gibbs free energies obtained from both computational protocols are in close agreement; they are positive and relatively small, indicating that there are no significant energetic barriers preventing the potential release of BTA molecules.

The HFLD analysis on the most stable conformers of the PAA–BTA and bPEI–BTA supramolecular complexes was carried out to further characterize the intermolecular interactions involved in supramolecular association.[55] The CBS-corrected interaction energies (see Methods in the ESI† for the detailed formula) were found to be +4.5 kcal mol^{-1} for PAA–BTA and +3.1 kcal mol^{-1} for bPEI–BTA, further supporting our hypothesis that the overall release process is energetically favorable. The noncovalent interaction (NCI) analysis for bPEI–BTA and PAA–bPEI supramolecular complexes was performed based on the obtained HFLD wavefunctions.[56,57] The NCI isosurfaces (green to red regions) revealed predominantly weak van der Waals contacts, consistent with the lack of strong stabilizing interactions (Fig. 5b and c). This outcome corroborates our previous findings and underscores the feasibility of BTA release under these conditions.

To examine the role of pH on supramolecular complexes stability, we evaluated the association Gibbs free energies of PAA and bPEI (without BTA) under both neutral (pH = 7) and acidic (pH < 7) conditions. The protonation states of PAA and bPEI were adjusted accordingly, and multiple conformers were considered to ensure comprehensive sampling (Fig. 5d and e). We also explored how the degree of bPEI protonation influences the stability of the bPEI–BTA supramolecular complexes. Three scenarios were assessed, corresponding to the protonation of

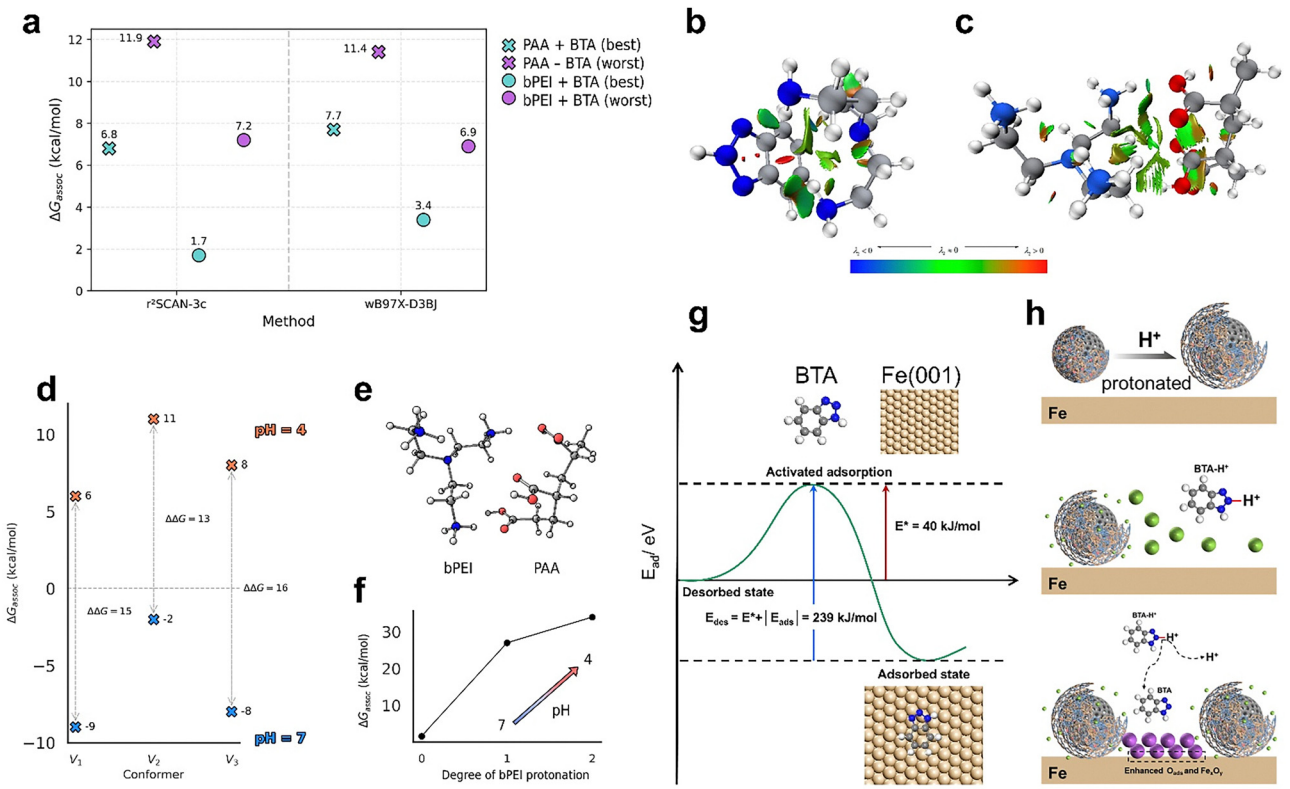

Fig. 5 Molecular release and absorption modelling. (a) Association Gibbs free energies of PAA and bPEI with BTA (ΔG_{assoc}) obtained from both computational protocols for the most favorable (best) and least favorable (worst) conformers in water solution. NCI surfaces for (b) bPEI–BTA and (c) PAA–bPEI. (d) Association Gibbs free energies for PAA–bPEI supramolecular complexes formation across different conformers in neutral (pH = 7) and acidic (pH < 7) environments. (e) Optimized model structure of one representative conformer. (f) Dependence of ΔG_{assoc} on the degree of bPEI protonation, showing increasing destabilization of hypothetical bPEI–BTA supramolecular complexes at higher protonation levels. (g) The optimized adsorption configurations and energy, with an adsorption energy (E_{ads}) of −2.06 eV. (h) The interrelated molecular release and absorption process.

one, two or all three NH_2 groups in bPEI. As shown in Fig. 5f, the association Gibbs free energy becomes progressively more positive as the protonation level increases, signaling a marked destabilization of the supramolecular complex. Moreover, at full protonation, the bPEI–BTA supramolecular complex failed to form, as the model system collapsed during the geometry optimization procedure and dissociated completely. Overall, the observed trend from DFT calculations aligns well with experimental findings, confirming that protonation plays a crucial role in triggering BTA release under acidic conditions.

We further performed DFT calculations on Fe(001) to provide quantitative evidence that BTA molecules can adsorb stably onto the Fe(001) surface (Fig. S20, ESI†). The optimized adsorption configurations and energies are shown in Fig. 5g, with an adsorption energy (E_{ads}) of −2.06 eV.[58] Based on the Arrhenius equation (see Methods in the ESI† for details), the residence time of the adsorbed species is approximately 17 years, indicating a stable adsorption of BTA on the Fe surface. As the protonation of bPEI increases under acidic conditions, the polyelectrolyte structure becomes destabilized and swollen, leading to increased RRMC coverage on the Fe surface (Fig. S21, ESI†). The resulting increased permeability accelerates BTA release, with BTA initially protonated to BTA-H^+ upon exposure to the acidic environment. When the coverage of BTA-H^+ on the Fe surface exceeds 1/4, deprotonation is initiated[59] (Fig. 5h). The deprotonated BTA forms more stable adsorption states, enhancing the persistence of chemisorbed species (*e.g.*, O_{ads} and Fe_xO_y). Collectively, protonated polyelectrolytes experience structural expansion upon exposure to acidic stimuli, resulting in the rapid swelling of microcapsules, accelerated BTA release and accumulation, which subsequently induces the deprotonation of BTA molecules. This process increases the adsorption and reaction rates of the corrosion inhibitor on the metal substrate, ultimately forming a more robust protective film for long-term corrosion protection.

Conclusions

In this work, we demonstrate the fabrication of robust pH-responsive microcapsules *via* an interfacial complexation–diffusion assembly strategy. The use of low-molecular-weight bPEI and high-molecular-weight PAA results in a dynamic, interpenetrating polyelectrolyte network. Owing to the use of cost-effective, commercially available reagents and mild reaction conditions, this approach is readily compatible with scale-up. Furthermore, the sol–gel/emulsion synthesis coupled with LBL deposition is both time-efficient and amenable to automation, enhancing its viability for industrial-scale production.

The resulting RRMCs afforded enhanced stability (with a reduced modulus of 1345 MPa) due to diffusion entanglement and covalent crosslinking and demonstrated tuneable pH-triggered changes in size and structure. These microcapsules exhibited a uniform spherical morphology (~728 nm in diameter) and substantial internal void, leading to a high encapsulation efficiency (~86%). The use of multiple deposition cycles allowed for precise control over shell thickness and release profiles. Notably, the RRMCs exhibited reversible pH responsiveness, swelling at pH ≤ 4 and contracting at higher pH levels, enabling the controlled release of BTA for metal corrosion inhibition over 8 hours in acidic environments. This reversible behaviour coupled with the microcapsules' enhanced stability, ensured periodic release and sustained functionality for up to 14 days. The promising corrosion inhibition properties of the RRMCs were demonstrated on metal substrates, forming a stable protective barrier under acidic conditions. Furthermore, DFT calculations revealed the interrelated process of BTA release from the RRMCs and its adsorption on the Fe surface, confirming that protonation was a key factor in triggering both BTA release and adsorption under acidic conditions. The microcapsule fabrication strategy described here offered significant potential for the development of dynamic responsive materials in a wide range of energy and environmental applications.

Author contributions

H. Z. and Z. S. contributed equally to this work. H. Z. conceived the idea. H. Z., Z. S. and R. C. designed and conducted the experiments, analysed the data. D. V. E., A. S. N. and E. V. S. carried out theoretical calculations. H. Z., D. G. S. and H. W. supervised the research and manuscript preparation. All authors approved the final version of the manuscript.

Conflicts of interest

There are no conflicts to declare.

Data availability

The data supporting this article have been included as part of the ESI.† The authors will supply the other relevant data in response to reasonable requests.

Acknowledgements

This work is financially supported by the National Key Research and Development Program of China (2022YFB3808800), the National Science Foundation for Distinguished Young Scholars of China (Grant No. 51925403), and the National Science Foundation of China (21676052 and 21606042). D. G. S. acknowledges EPSRC projects EP/Y030397/1 and EP/X039773/1. Grant RSF 24-13-00355 is acknowledged for computational part. We are grateful to Y. C. Kang for his assistance with the molecule adsorption calculations, and J. Q. Ning for his assistance with the AFM characterization.

Notes and references

1 K. M. G. Langie, K. Tak, C. Kim, H. W. Lee, K. Park, D. Kim, W. Jung, C. W. Lee, H. S. Oh, D. K. Lee, J. H. Koh, B. K. Min, D. H. Won and U. Lee, *Nat. Commun.*, 2022, **13**, 1–10.

2 N. Dutta and S. C. Peter, *J. Am. Chem. Soc.*, 2025, **147**, 9836–9843.
3 B. Chang, H. Pang, F. Raziq, S. Wang, K. W. Huang, J. Ye and H. Zhang, *Energy Environ. Sci.*, 2023, **16**, 4714–4758.
4 Q. Lyu, J. Tan, L. Li, Y. Ju, A. Busch, D. A. Wood, P. G. Ranjith, R. Middleton, B. Shu, C. Hu, Z. Wang and R. Hu, *Energy Environ. Sci.*, 2021, **14**, 4203–4227.
5 S. Mura, J. Nicolas and P. Couvreur, *Nat. Mater.*, 2013, **12**, 991–1003.
6 C. J. Kim, F. Ercole, J. Chen, S. Pan, Y. Ju, J. F. Quinn and F. Caruso, *J. Am. Chem. Soc.*, 2022, **144**, 503–514.
7 Z. Liu, W. Wang, R. Xie, X. J. Ju and L. Y. Chu, *Chem. Soc. Rev.*, 2016, **45**, 460–475.
8 Y. Lu, A. A. Aimetti, R. Langer and Z. Gu, *Nat. Rev. Mater.*, 2016, **2**, 1–17.
9 W.-C. Liao, I. Willner, W. Liao and I. Willner, *Adv. Funct. Mater.*, 2017, **27**, 1702732.
10 C. J. T. Cox, J. Hale, P. Molinska and J. E. M. Lewis, *Chem. Soc. Rev.*, 2024, **53**, 10380–10408.
11 M. A. Rahim, K. Kempe, M. Müllner, H. Ejima, Y. Ju, M. P. Van Koeverden, T. Suma, J. A. Braunger, M. G. Leeming, B. F. Abrahams and F. Caruso, *Chem. Mater.*, 2015, **27**, 5825–5832.
12 W. Xu, Z. Lin, S. Pan, J. Chen, T. Wang, C. Cortez-Jugo and F. Caruso, *Angew. Chem., Int. Ed.*, 2023, **62**, e202312925.
13 K. Zeng, F. Doberenz, Y. T. Lu, J. P. Nong, S. Fischer, T. Groth and K. Zhang, *ACS Appl. Mater. Interfaces*, 2022, **14**, 48384–48396.
14 Z. Zheng, J. Jin, G. K. Xu, J. Zou, U. Wais, A. Beckett, T. Heil, S. Higgins, L. Guan, Y. Wang and D. Shchukin, *ACS Nano*, 2016, **10**, 4695–4703.
15 S. Correa, K. Y. Choi, E. C. Dreaden, K. Renggli, A. Shi, L. Gu, K. E. Shopsowitz, M. A. Quadir, E. Ben-Akiva and P. T. Hammond, *Adv. Funct. Mater.*, 2016, **26**, 991–1003.
16 E. Guzmán, R. G. Rubio and F. Ortega, *Adv. Colloid Interface Sci.*, 2020, **282**, 102197.
17 Q. An, T. Huang and F. Shi, *Chem. Soc. Rev.*, 2018, **47**, 5061–5098.
18 J. Zhang, R. J. Coulston, S. T. Jones, J. Geng, O. A. Scherman and C. Abell, *Science*, 2012, **335**, 690–694.
19 C. E. Hansen, D. R. Myers, W. H. Baldwin, Y. Sakurai, S. L. Meeks, L. A. Lyon and W. A. Lam, *ACS Nano*, 2017, **11**, 5579–5589.
20 D. Grigoriev, E. Shchukina and D. G. Shchukin, *Adv. Mater. Interfaces*, 2017, **4**, 1600318.
21 R. Heuberger, G. Sukhorukov, J. Vörös, M. Textor and H. Möhwald, *Adv. Funct. Mater.*, 2005, **15**, 357–366.
22 E. M. Foster, E. E. Lensmeyer, B. Zhang, P. Chakma, J. A. Flum, J. J. Via, J. L. Sparks and D. Konkolewicz, *ACS Macro Lett.*, 2017, **6**, 495–499.
23 X. Li, D. Zhao, K. J. Shea, X. Li and X. Lu, *Mater. Horiz.*, 2021, **8**, 932–938.
24 T. Kruk, K. Chojnacka-Górka, M. Kolasińska-Sojka and S. Zapotoczny, *Adv. Colloid Interface Sci.*, 2022, **310**, 102773.
25 Z. Dai, X. Yang, F. Wu, L. Wang, K. Xiang, P. Li, Q. Lv, J. Tang, A. Dohlman, L. Dai, X. Shen and L. You, *Nat. Commun.*, 2021, **12**, 1–9.
26 B. M. Discher, Y. Y. Won, D. S. Ege, J. C. M. Lee, F. S. Bates, D. E. Discher and D. A. Hammer, *Science*, 1999, **284**, 1143–1146.
27 S. Honda, T. Yamamoto and Y. Tezuka, *Nat. Commun.*, 2013, **4**, 1–9.
28 F. M. Haque and S. M. Grayson, *Nat. Chem.*, 2020, **12**, 433–444.
29 M. Skiba, R. R. Reszegi, Y. Huang, S. Roy, J. Han, D. Brückner, C. Sanchez-Cano, Y. Zhao, M. Hassan, N. Feliu, G. Falkenberg and W. J. Parak, *Adv. Funct. Mater.*, 2025, **35**, 2408539.
30 J. Li, B. V. Parakhonskiy and A. G. Skirtach, *Chem. Commun.*, 2023, **59**, 807–835.
31 H. Zhou, R. Cheng, M. Quarrell and D. Shchukin, *J. Colloid Interface Sci.*, 2023, **638**, 403–411.
32 H. Cui, N. Pan, W. Fan, C. Liu, Y. Li, Y. Xia, K. Sui, H. Cui, N. Pan, W. Fan, C. Liu, Y. Li, Y. Xia and K. Sui, *Adv. Funct. Mater.*, 2019, **29**, 1807692.
33 G. Bian, N. Pan, Z. Luan, X. Sui, W. Fan, Y. Xia, K. Sui and L. Jiang, *Angew. Chem., Int. Ed.*, 2021, **60**, 20294–20300.
34 G. Ibarz, L. Dähne, E. Donath and H. Möhwald, *Chem. Mater.*, 2002, **14**, 4059–4062.
35 W. Mendez-Ortiz, K. J. Stebe and D. Lee, *ACS Nano*, 2022, **16**, 21087–21097.
36 L. Du, S. Liao, H. A. Khatib, J. F. Stoddart and J. I. Zink, *J. Am. Chem. Soc.*, 2009, **131**, 15136–15142.
37 H. S. Jeong, E. Kim, J. P. Park, S. J. Lee, H. Lee and C. H. Choi, *J. Controlled Release*, 2023, **356**, 337–346.
38 T. Mauser, C. Déjugnat, H. Möhwald and G. B. Sukhorukov, *Langmuir*, 2006, **22**, 5888–5893.
39 P. Tzeng, C. R. Maupin and J. C. Grunlan, *J. Membr. Sci.*, 2014, **452**, 46–53.
40 T. Mauser, C. Déjugnat and G. B. Sukhorukov, *Macromol. Rapid Commun.*, 2004, **25**, 1781–1785.
41 B. Ihor Tokarev, S. Minko, I. Tokarev and S. Minko, *Adv. Mater.*, 2010, **22**, 3446–3462.
42 X. Liu, D. Appelhans and B. Voit, *J. Am. Chem. Soc.*, 2018, **140**, 16106–16114.
43 G. Cai, M. Ding, Q. Wu and H.-L. Jiang, *Natl. Sci. Rev.*, 2020, **7**, 37–45.
44 Q. Zhang, P. Feng, J. Shi and H. Wang, *Corros. Sci.*, 2022, **207**, 110572.
45 C. K. Tan and D. J. Blackwood, *Corros. Sci.*, 2003, **45**, 545–557.
46 B. S. Hou, Q. H. Zhang, Y. Y. Li, G. Y. Zhu and G. A. Zhang, *Corros. Sci.*, 2020, **166**, 108442.
47 F. Chiter, Y. Bulteau, P. Bonin, N. Pébère and C. Lacaze-Dufaure, *Corros. Sci.*, 2024, **233**, 112104.
48 D. Iravani, A. Farhadian, R. Sharifi, A. Berisha, A. Rahimi, A. Shaabani, Y. Qiang, A. A. Javidparvar, D. A. Martyushev and E. Akbarinezhad, *Corros. Sci.*, 2025, **246**, 112712.
49 F. X. Perrin, N. Leibl, L. Belec, A. Fahs, N. Caussé and N. Pébère, *Corros. Sci.*, 2025, **242**, 112558.
50 Z. Chen, L. Huang, G. Zhang, Y. Qiu and X. Guo, *Corros. Sci.*, 2012, **65**, 214–222.
51 A. Moncho-Jorda, A. B. Jodar-Reyes, M. Kanduc, A. German-Bellod, J. M. Lopez-Romero, R. Contreras-Caceres, F. Sarabia,

M. García-Castro, H. A. Perez-Ramirez and G. Odriozola, *ACS Nano*, 2020, **14**, 15227–15240.
52 J. Gorges, S. Grimme and A. Hansen, *Phys. Chem. Chem. Phys.*, 2022, **24**, 28831–28843.
53 S. Grimme, A. Hansen, S. Ehlert and J. M. Mewes, *J. Chem. Phys.*, 2021, **154**, 64103.
54 J. Da Chai and M. Head-Gordon, *Phys. Chem. Chem. Phys.*, 2008, **10**, 6615–6620.
55 A. Altun, F. Neese and G. Bistoni, *J. Chem. Theory Comput.*, 2019, **15**, 5894–5907.
56 E. R. Johnson, S. Keinan, P. Mori-Sánchez, J. Contreras-García, A. J. Cohen and W. Yang, *J. Am. Chem. Soc.*, 2010, **132**, 6498–6506.
57 T. Lu, *J. Chem. Phys.*, 2024, **161**, 82503.
58 A. Kokalj, *Corros. Sci.*, 2022, **196**, 109939.
59 A. Kokalj and M. Dlouhy, *Corros. Sci.*, 2022, **209**, 110680.